

The Effect of Lubricant Viscosity on Nucleation for Water Condensation on Lubricant-Infused Surfaces

Jianxing Sun^a, Vivek V. Manepalli^{a,b}, Xinyu Jiang^a, Patricia B. Weisensee^{a,c,*}

a. Department of Mechanical Engineering & Materials Science, Washington University in St. Louis, USA

b. Department of Mechanical Engineering, Birla Institute of Technology & Science, Pilani – Hyderabad, India

c. Institute of Materials Science and Engineering, Washington University in St. Louis, USA

* corresponding author: p.weisensee@wustl.edu

Abstract Lubricant-infused surfaces (LIS) can promote stable dropwise condensation and improve heat transfer rates due to a low nucleation energy barrier and high droplet mobility. Although significant dependences of microdroplet mobility and droplet coalescence on lubricant viscosity have been reported, the influence of lubricant viscosity on condensation is considerably less studied, and the spatial preference for nucleation on a non-uniform lubricant film on LIS during condensation is not well understood. Previous work demonstrated a dynamic re-distribution of the lubricant film during condensation, leading to oil-rich and oil-poor regions. In this work, we study water vapor condensation with nitrogen as carrier gas on LIS infused with Krytox oils of different viscosity within a custom-built chamber at various gas temperatures. We combine high-speed imaging and optical microscopy to determine the apparent (droplet size $\sim 1 \mu\text{m}$) nucleation rate and density on LIS. We show that nucleation predominantly occurs in oil-poor regions where the oil-vapor interfacial temperature is lower than in oil-rich regions. This small temperature difference is enough to cause a significantly lower nucleation free-energy barrier in the oil-poor regions, leading to enhanced nucleation. The relative area ratio of oil-poor regions to total surface area, *i.e.*, preferred area for nucleation, can be tailored between 11% and 19% by changing the lubricant viscosity from 1627 to 73 cP. We statistically analyze the influence of lubricant viscosity on the new emerging droplets on LIS at a wide range of gas-substrate temperature differences. The results show that the nucleation rate density dramatically increases with this temperature difference. More importantly, a strong dependence of nucleation rate density on lubricant viscosity is discovered, which means that higher heat transfer rates can potentially be achieved by lowering lubricant viscosity. We attribute the enhanced nucleation primarily to enhanced droplet mobility and more frequent surface refreshing at lower lubricant viscosity.

Keywords Lubricant-infused surface; LIS; Dropwise condensation; Nucleation rate; Nucleation density

1 Introduction

Achieving dropwise condensation is of continued interest and desirable in many industrial applications, such as water-harvesting [1], desalination [2,3], power generation [4], and thermal management [5], due to higher heat transfer performance and water collection rates. Although the presence of even a small amount of non-condensable gases (NCG) will significantly reduce the condensation heat transfer rate [6], water vapor condensation with NCG is commonly found in many of these applications. In recent decades, many efforts have been dedicated to creating various non-wettable engineered surfaces, such as superhydrophobic [7,8], hybrid [9], and lubricant-infused surfaces (LIS) [10], to enable the formation of discrete condensate droplets and to enhance water shedding from the surface once condensed. Notably, LIS can promote stable dropwise condensation of water and low surface energy liquids [11,12]. The droplets can shed from substrates at relatively smaller critical diameters under gravity due to their extremely low contact angle hysteresis. At the same time, onset of heterogeneous water nucleation intrinsically occurs more easily on a soft or liquid surface than a solid one under the same conditions. Many researchers have shown through theoretical modeling that the energy barrier for heterogeneous nucleation on a fluid surface is lower than on a rigid surface based on a Gibbsian thermodynamic surface analysis [13,14]. Sokuler and co-workers experimentally investigated the nucleation and the growth of condensing water droplets on soft poly(dimethyl siloxane) (PDMS) films with varying elasticity and viscosity. They found that nucleation is faster on a soft surface than on a hard one due to a reduced activation barrier for nucleation [15]. All of these benefits can potentially improve nucleation and thereby significantly enhance the heat transfer performance on LIS compared to solid hydrophobic surfaces [16,17], since microscopic condensate droplets ($< 10 \mu\text{m}$) account for approximately 75% of the total heat transfer during dropwise condensation [18].

In spite of its importance, the interplay between the thin lubricant film and nucleation on LIS remains elusive. On a solid surface, droplets are thought to nucleate primarily on topographical and chemical defects, such as cavities and hydrophilic sites [19,20], and grow by direct vapor diffusion and coalescence with other droplets. However, nucleation on LIS is fundamentally unique due to the existence of a layer of a molecularly smooth lubricant film between water vapor and the solid superhydrophobic surface. This layer of lubricant film, however, potentially facilitates water nucleation, as discussed above. The preferred location for nucleation has undergone intense debates. Xiao *et al.* assumed that vapor diffuses through a thin layer of lubricant covering hydrophilic sites of bi-philic pillars and nucleates at the lubricant-solid interface [16]. Anand *et al.* argued, based on theoretical considerations of vapor transport in liquids, that – while thermodynamically (*i.e.*, at equilibrium) favorable – nucleation at the lubricant-solid interface is not likely due to the limited solubility of vapor in the lubricant [21]. They proposed that droplets nucleate at the lubricant-vapor interface, and later move into the lubricant due to cloaking and capillary forces. Using 3D laser scanning confocal microscopy, Kajiyama *et al.* confirmed that droplets nucleate at the lubricant-vapor interface, preferentially at the edges of pillars, where the lubricant curvature decreases the energy barrier for nucleation [22]. Despite these previous efforts, the question remains whether on a microscopically flat and chemically homogeneous surface, *i.e.*, a substrate with only nanostructures to lock the lubricant in place [23], water vapor will uniformly nucleate on the lubricant-vapor interface of a non-uniformly distributed oil film, or whether there still exists an in-plane spatial preference for nucleation. It is well known that on LIS lubricant rises at the sides of droplets to form lubricant ridges due to capillary forces [24–27]. On the macroscale, the size of this lubricant ridge surrounding a millimetric droplet is very small compared to the size of the droplet. However, in our recent work [28], using interference microscopy, we observed comparatively large oil menisci surrounding post-nucleation microdroplets on LIS, effectively creating oil-rich regions surrounding these droplets and droplet clusters. Due to conservation of mass, oil-poor regions

formed in the droplet-empty spaces. Therefore, a microscopically uneven distribution of the lubricant film is common during condensation, which is expected to influence the spatial preferences for nucleation.

Caused by this non-uniform lubricant layer, microdroplets were able to robustly self-propel long distances and thereby coalesce with neighboring droplets on a frequent basis, which assisted the refreshing for re-nucleation of the surface along the trajectories. The movement velocity and frequency were heavily dependent on the lubricant viscosity [28]. Similarly, Anand *et al.* observed that the size distribution of condensate droplets at early times and the area fraction of droplet coverage are highly contingent upon lubricant viscosity [21]. Macroscopically, the distribution of droplet sizes on LIS has been reported to be independent of lubricant viscosity for steady-state condensation [18], however, lower viscosity oil-infused smooth surfaces showed a higher condensation heat transfer coefficient than those with oil of higher viscosity [29]. Based upon these observations, we hypothesize here that there exists a competition of two opposing forcings: 1) The spatially non-uniform distribution of the oil film on LIS might lead to a decreased area-availability for droplet nucleation, with nucleation being limited to oil-poor regions, and hence a reduction in dropwise condensation efficiency as compared to solid hydrophobic surfaces. 2) A decreased nucleation energy barrier and a (viscosity-dependent) higher droplet mobility and coalescence frequency might enhance the nucleation and heat transfer efficiency of LIS compared to a hydrophobic surface. Indeed, as we will show below, the existence of wetting ridges greatly influences the nucleation distribution, however, there exists a non-trivial dependence on lubricant viscosity due to its influence on droplet mobility and droplet coalescence.

In this paper, in order to experimentally examine the interplay of lubricant dynamics and nucleation during condensation, we conducted water vapor condensation experiments in the presence of non-condensable gases on Krytox-infused surfaces in a custom-designed environmental chamber with controllable gas and substrate temperatures at atmosphere pressure. We refer to the smallest visible droplets (approximately 1 μm in diameter) as “nuclei”, since 1) coalescence is typically thought of as becoming important only for microdroplets [30] and 2) nanodroplets account for a negligible amount of heat towards the overall heat transfer, and are hence not relevant for the purpose of this work. The spatial preference of nucleation was investigated using high-speed imaging and optical microscopy. A combination of thermodynamic analysis of the nucleation energy barrier and infrared (IR) thermal imaging of the oil-vapor interface on LIS during condensation were performed to interpret the observed nucleation preferences. The area ratio of oil-poor regions, *i.e.*, the favorable area for nucleation, to the total surface area on LIS was analyzed at different times during condensation. We also examined the dependence of the formation and area of oil-poor regions on lubricant viscosity. Finally, we conducted condensation experiments on LIS with different lubricant viscosities at a wide range of temperature differences between the vapor–N₂ mixture and the substrate. To better evaluate condensation and heat transfer rates, we propose that it is necessary to examine the transient (re-)nucleation density during longer time intervals, and introduce the concept of a nucleation rate density ($\#/\text{m}^2\cdot\text{s}$), which takes into account the area availabilities for re-nucleation (*i.e.*, a spatial component) and kinetics of nucleation (*i.e.*, a temporal component). The average nucleation rate density in a complete condensation cycle is presented to demonstrate the overall nucleation and condensation process. We conducted a statistical analysis over many such cycles to elucidate the relationship between nucleation rate density, lubricant viscosity, and the gas-substrate temperature difference. These findings will advance our understanding of the mechanism of droplet nucleation on LIS, competing factors during condensation, and help inform the selection of a lubricant for LIS to achieve higher nucleation rate densities and condensation heat transfer rates.

2 Materials and methods

2.1 Preparation of lubricant-infused surfaces

The substrate was obtained by cutting a plain microscope glass slide (Thermo Scientific) into pieces (25 mm × 25 mm), which were then rinsed with acetone, isopropanol, and de-ionized (DI) water in sequence, and dried with compressed N₂. Subsequently, the cleaned glass surface was sprayed with Glaco Mirror Coat Zero (soft 99 Co., Japan) and then placed in the fume hood at room temperature for at least 1 hour. Glaco is a commercially available superhydrophobic agent consisting of the suspension of functionalized silica nanoparticles (~ 40 nm) in alcohol. This process renders a layer of relatively uniform porous nanostructure with a thickness of ~ 1 μm on the surface, as shown in the top view and cross-sectional scanning electron microscope (SEM) images in **Figure 1a-c**. The contact angle of DI water on the Glaco-coated glass slide is $165 \pm 3^\circ$ with negligible hysteresis. In this work, Krytox GPL oils were chosen as the infused liquid, featuring a large range of viscosities at similar surface tensions of $\gamma_{ov} = 17 \pm 1$ mN/m in vapor and $\gamma_{do} = 53$ mN/m in water [27]. To obtain the lubricant-infused surface, the nanostructured surface was impregnated with Krytox oils *via* spin coating. Based on the spin coating model developed by Emslie [31], the film thickness scales as $d_{oil} \sim (\mu/t\omega^2)^{1/2}$, where μ is the oil viscosity, t is the total rotating time of the sample, and ω is the angular velocity of the sample. The revolutions per minute (RPM) were set for different viscosity oils as shown in **Table 1**. The thickness of the initial oil film was measured to 10 ± 1.5 μm for all viscosities using high-speed interferometry, following the technique discussed in our previous work [28]. The top-view interference microscopy image in **Figure 1d** shows a fresh LIS sample just prior to water vapor condensation, highlighting the uniform oil film thickness. The wide-spaced interference fringes are caused by the slight tilt of the sample. Any defects or condensate droplets (as, for example, outlined with the dashed rectangle in the center of the image, which is about to poke through the interface) protruding from the oil film would disturb the uniform interference patterns. For a millimetric water droplet, the apparent contact angle on LIS is approximately 90° . Microscopically, Krytox GPL oils cloak water, *i.e.*, spread on the water droplets and the superhydrophobic sample due to positive spreading coefficients [21,25,32]: $S_{do(v)} = \gamma_{dv} - \gamma_{ov} - \gamma_{do} > 0$ and $S_{os(d)} = \gamma_{ds} - \gamma_{os} - \gamma_{do} > 0$, where γ_{dv} , γ_{ov} , γ_{do} , γ_{os} and γ_{ds} denote the interfacial energies between water droplet-vapor, oil-vapor, water droplet-oil, oil-solid and water droplet-solid, respectively [24,33]. For comparison, solid hydrophobic samples were also prepared by coating the cleaned glass with a layer of hexadecyltrimethoxysilane (HTMS) with advancing and receding contact angles of $111 \pm 3^\circ$ and $97 \pm 3^\circ$, respectively.

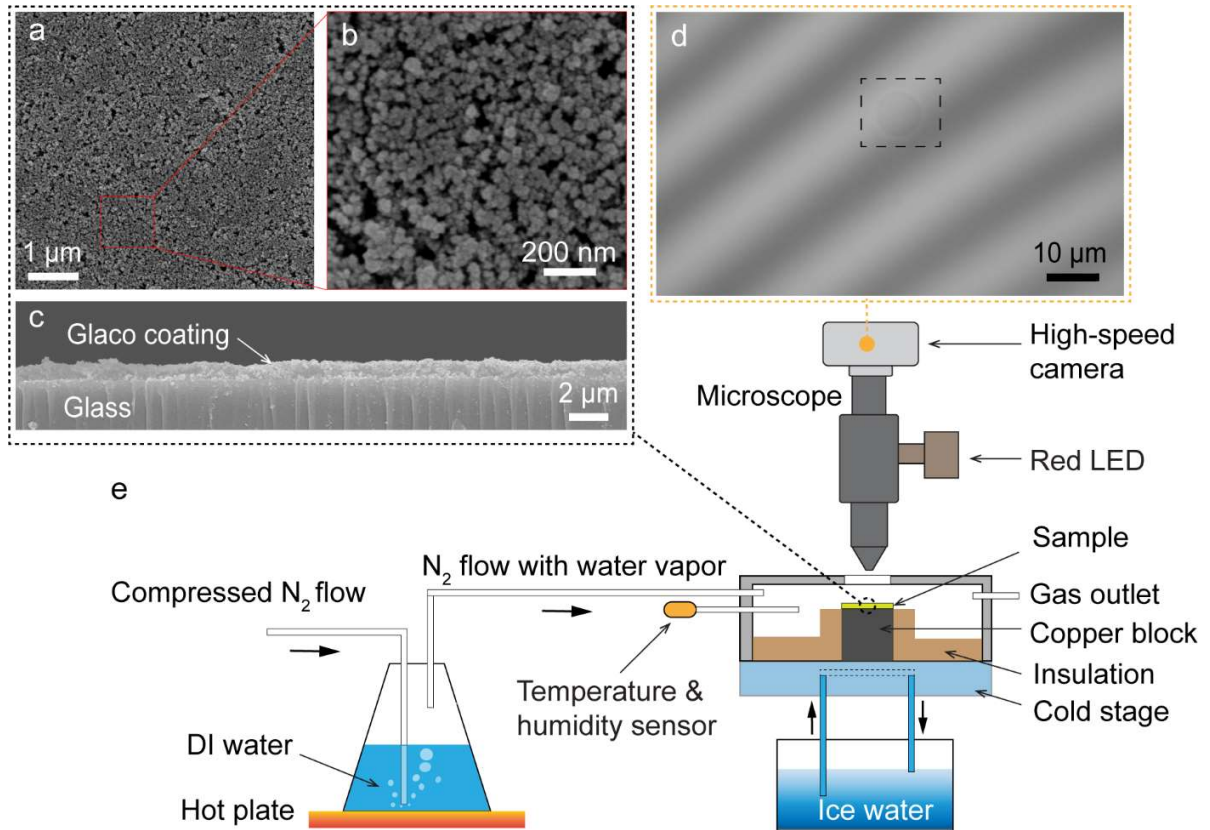


Figure 1 Experimental set-up and characterization of nanostructured surface before and after lubricant impregnation. (a-c) Scanning electron microscope (SEM) images of the Glaco superhydrophobic coating prior to oil infusion from top and cross-sectional views. (d) Interferometry image of a fresh LIS sample at the start of gentle condensation. The widely spaced interference patterns are caused by a slight tilt of the sample. A condensed microdroplet about to protrude the oil-vapor interface appears in the center of the dashed rectangle. (e) Schematic of the experimental condensation apparatus.

2.2 Water vapor condensation experiments

We conducted water vapor condensation experiments on LIS with varying lubricant viscosity at a series of gas-substrate temperature differences, where N_2 served as carrier gas. As shown in **Figure 1e**, a LIS sample was placed on a copper block inside a custom-built chamber. A cold plate connected to the copper block was maintained at a constant temperature ($T_s \approx 276 \pm 1.5$ K) by the circulation of ice water. A flask containing DI-water was heated on a hot plate (Thermo Fisher Scientific). Compressed nitrogen gas was supplied to the bottom of the flask at a flow rate of 12.5 ± 1 liters per minute (LPM), controlled by a flowmeter (NFM-TT, Turbo Torch), and then N_2 mixed with hot water vapor was guided into the chamber through insulated plastic tubes. A lower flow rate, 4 ± 1 LPM, was set to obtain slow condensation for thermal imaging measurements. The chamber might contain other non-condensable components of air, such as O_2 and CO_2 , but their concentrations are expected to be negligible. The degrading heat transfer performance of dropwise condensation with NCG is mainly attributed to the existence of the diffusion layer and its resistance of the vapor–NCG boundary layer, less to the composition of the gas [34]. Before running condensation experiments, we first calibrated the hot plate temperature to obtain the target temperatures of

the vapor-saturated nitrogen gas. Then, for every condensation experiment, we set the hot plate temperature and waited for the system to reach steady, before turning on the water vapor supply to the chamber. The temperature and relative humidity (RH) in the chamber were monitored by a temperature and RH probe (PCMini52, MICHELL Instruments) with an accuracy of $\pm 1\text{K}$ and $\pm 1\%$ at $RH = 20\% - 90\%$, $\pm 5\%$ at $RH > 90\%$, respectively. The relative humidity value was close to 100% for all experiments. The nucleation dynamics were monitored under an upright DIY Cerna Microscope (Thorlabs) equipped with brightfield objectives ($10\times$, $50\times$, $100\times$ L Plan SLWD). Videos were obtained using a Photron FASTCAM Mini AX200 high-speed camera at 60–1000 frames per second (fps). For the investigation of the time evolution of the nucleation rate density on LIS (section 3.3), the chamber was oriented vertically, and we focused on the center of the sample. The sample surface was naturally swept by large sliding droplets due to gravity. In the experiments for studying the effect of lubricant viscosity on the nucleation rate density (section 3.4), the chamber was placed horizontally. Once we observed the occurrence of large condensate droplets with a diameter of over $700\ \mu\text{m}$ (spanning about two times the field-of-view under the $50\times$ objective, $379\times 379\ \mu\text{m}$), we stopped collecting data and then gently tilted the chamber to a vertical position to let droplets shed, leaving a fresh area for the next cycle of nucleation, growth, coalescence, and droplet shedding (“sweeping cycle”).

Table 1 Physical properties at room temperature and corresponding spin coating parameters.

Lubricant	Viscosity ν [cP]	Surface tension γ_{ov} [mN/m]	Thermal conductivity [W/m · K]	RPM	Time [s]
Krytox GPL102	73	17 ± 1 [27]	0.08 – 0.09	600	120
Krytox GPL104	350	17 ± 1 [27]	0.08 – 0.09	1160	120
Krytox GPL106	1627	17 ± 1 [27]	0.08 – 0.09	2700	120
DI water	1	72	0.6	N/A	N/A

Note: The viscosity and thermal conductivity information of Krytox oils are obtained from the manufacturer

2.3 Image processing for identifying oil-poor regions

To obtain the initial re-distribution and information on the area-ratio of oil-poor regions, we conducted experiments with low magnification ($10\times$) at 250 fps. We then extracted one frame of the videos every 5 seconds to perform a detailed image analysis. Image sequences were first processed by MATLAB to eliminate any unevenness of illumination and to improve image quality. Then, the corrected image sequences in grayscales were cropped into 500×500 pixels ($0.86\ \text{mm}^2$) to eliminate vignetting, as shown in Figure 2a. The gray value is inversely proportional to oil film thickness, as less light is absorbed and scattered by the thinner oil layer. Figure 2b shows the change of grayscale values along the cyan line in Figure 2a. The grayscale values between points B and C are uniformly high, corresponding to oil-poor regions. However, the value decreases between points B and A, since an oil meniscus with an exponential height profile surrounds the droplet. We define this region as oil-rich. We used scanning confocal fluorescence microscopy (Zeiss LSM 880 Airyscan Confocal Microscope) to measure the film thickness in oil-rich and oil-poor regions from water condensation on Glaco-coated glass infused with vacuum pump oil (Cole Parmer cP500). The oil was dyed with Lumogen F Red 305 (BASF Colors & Effects). In this case,

as shown in **Figure 2c**, the oil film thickness in the oil-poor regions evenly approximated to $2.5 \pm 0.3 \mu\text{m}$. In the oil-rich regions, an oil film thickness gradient existed because of the oil meniscus shape, with a median value of $6 \pm 0.3 \mu\text{m}$ (surrounding a droplet with a diameter of $28 \pm 2 \mu\text{m}$). While the absolute thickness for other oils and process conditions might be different from these, insights on the relative distribution of oil thicknesses applies to those cases as well. The measurement results gave us confidence in the method of identifying oil-poor regions based on the gray values. Then, by adjusting the threshold of the grayscale for each video separately to the value of point B in ImageJ, the image sequences are converted into binary images: black for oil-poor regions and white for oil-rich regions and droplets, as seen in **Figure 2d**. The bright spots in the center of droplets were removed by an image segmentation process. Finally, we used the particle analysis function in ImageJ to calculate the total area of black patches in each frame and relate it to the total area to obtain the ratio of oil-poor regions. This area fraction was calculated for a minimum of 17 different samples of the same lubricant and averaged so that the final values converge to a mean value and reduce error.

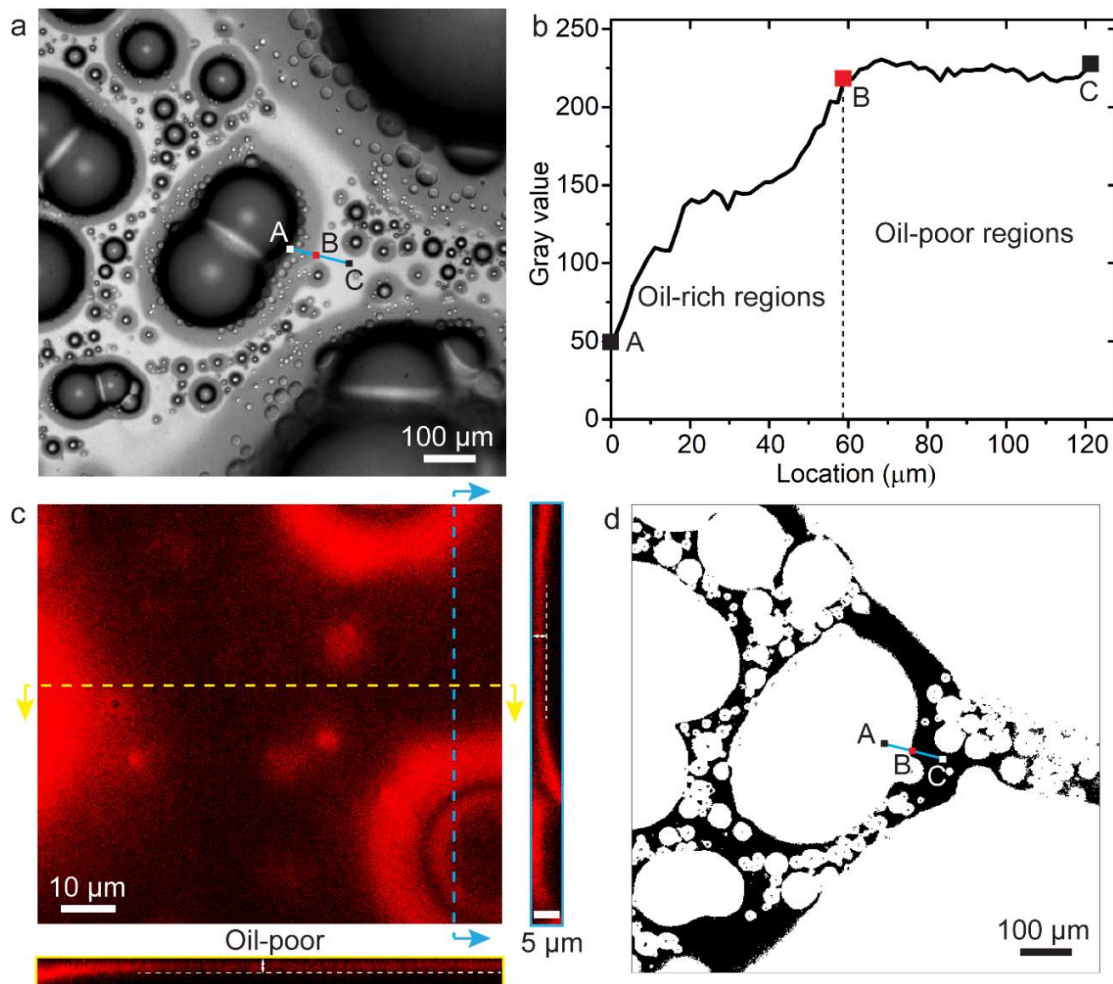


Figure 2 Oil film characterization. (a) A grayscale image of condensation and oil re-distribution on LIS. The cyan color line spans oil-rich regions (point A) to oil-poor regions (point C). Point B marks the transition point between the two regions. (b) Grayscale values of the line A-B-C in (a). (c) Characterization of the oil film thickness using 3D confocal microscopy on a Glaco-coated glass infused with vacuum pump oil dyed with Lumogen F Red 305. Orthogonal views of the image stack show the uneven oil film distribution (oil-rich and oil-poor regions). (d) The binary image after applying the grayscale threshold from point B to image (a).

2.4 Statistical analysis of nucleation rate density

New samples were used for each experiment with a certain combination of lubricant viscosity and gas temperature, and every experiment was repeated at least three times. We recorded three artificial sweeping cycles for each sample with a 50× objective lens and observed 5–7 locations in each sweep. A sweeping cycle is the time interval from the formation of distinct oil-rich and oil-poor regions to the moment that condensate droplets grow to a certain size and are removed from the surfaces (if vertically placed they naturally shed due to gravity). At each location, a video was recorded with a duration of about 12 seconds. Three randomly selected one-second long segments were extracted from each video and the number of nucleation events were counted manually at every frame. The size of the region of interest was 900×950 pixels, that is, 0.117 mm^2 for the 50× objective. Additional data point analysis was adopted when existing data showed a large spread. Finally, we averaged the results from every data point within different sweeping cycles for each combination of lubricant viscosity and gas temperature. It is extremely challenging to experimentally characterize the nucleation rate density, since the nucleation process originates at a molecular scale with cluster sizes of a few nanometers. Here, we counted the number of nucleated droplets once they became visible. The smallest detectable droplet with the 50× objective is $1.85 \pm 0.37 \text{ }\mu\text{m}$. Using the 100× objective lens, we were able to detect droplets with approximately $1 \text{ }\mu\text{m}$ in diameter and observed that droplets smaller than $2 \text{ }\mu\text{m}$ rarely coalesce with neighboring droplets. Therefore, it is safe to use the 50× objective to increase the field of view at the expense of resolution and approximate the number of the smallest microdroplets to be representative of the number of nucleating droplets. After each sweeping cycle, we intentionally excluded the first generation of nuclei, as the oil film has not yet re-distributed and hence the nucleation process is nearly uniform regardless of lubricant viscosity. Instead, we waited for the oil film to re-distribute into oil-poor and oil-rich regions and condensation reached a quasi-steady state. We also acknowledge that nucleation might be undercounted due to shedding of big droplets on the surface before nucleation becomes visible with our method. However, this difference is nearly negligible for high viscous lubricants due to a lower mobility of droplets. To a certain extent, our results will underestimate the real nucleation rate density, however, are well suited to elucidate the general effect of lubricant viscosity on nucleation and condensation dynamics.

3 Results

3.1 Preferred areas for nucleation: oil-poor regions

Due to limited vapor diffusion in an oil film as well as the low nucleation energy barrier of a liquid interface, water nucleation has been assumed to happen on the oil-vapor interface of LIS [13,21]. However, the in-plane spatial preference for nucleation has been less examined. As schematically shown in [Figure 3a](#), on a fresh LIS with a nanostructured substrate, uniform nucleation will occur on the flat oil-vapor interface (also compare to $t = 30 \text{ s}$ of [Figure 5c](#)). Subsequently, the droplets move into the lubricant due to oil cloaking and capillary forces and post-nucleation microdroplets grow *via* coalescence with other emerged droplets (not shown here). Oil menisci form around numerous microdroplets that protrude from the oil film. As the droplets move across the surface and coalesce with neighboring droplets, the initially uniform lubricant film redistributes into distinct microscopic oil-rich and oil-poor regions [28]. Then, during the remainder of the condensation process, the distribution of oil-rich and oil-poor regions changes dynamically due to robust self-propulsion of microdroplets. A more detailed description of the dynamic oil film re-distribution can be found in [Section 3.2](#). One question that naturally arises is whether the dynamic lubricant film affects the lateral spatial preference of water nucleation. To investigate the interplay of nucleation and the dynamic

oil film during condensation, here we conducted condensation experiments on LIS with Krytox GPL 104. In the optical image sequences of **Figures 3b, c**, oil-poor regions (marked with red ellipses) are characterized by having a brighter color, as less light is absorbed and scattered by the thin oil layer compared to a thicker one, and wide interference fringes. At $t = 0.24$ s, we see that the emergence of new droplets is limited to the oil-poor regions, and droplets coalesce with neighboring ones to create fresh oil-poor regions. **Figure 3c** presents a relatively larger view of a characteristic condensation process using the $20\times$ objective. To obtain the two images, we conducted a condensation experiment to generate the non-uniform oil distribution. Then, condensation was halted by turning off the supply of hot vapor- N_2 gas mixture and coolant circulation, and microdroplets in oil-poor regions were removed by evaporation or self-propulsion towards big droplets. Extra caution was needed to prevent evaporation of larger droplets sitting in the center of oil-rich regions. Then, we turned coolant and gas back on in sequence. The emergence of condensation nuclei on the sample surface was imaged using high-speed imaging at 500 fps to capture the first emerging droplets. We observe that nucleation (circled in yellow by ImageJ) is again confined to the oil-poor regions.

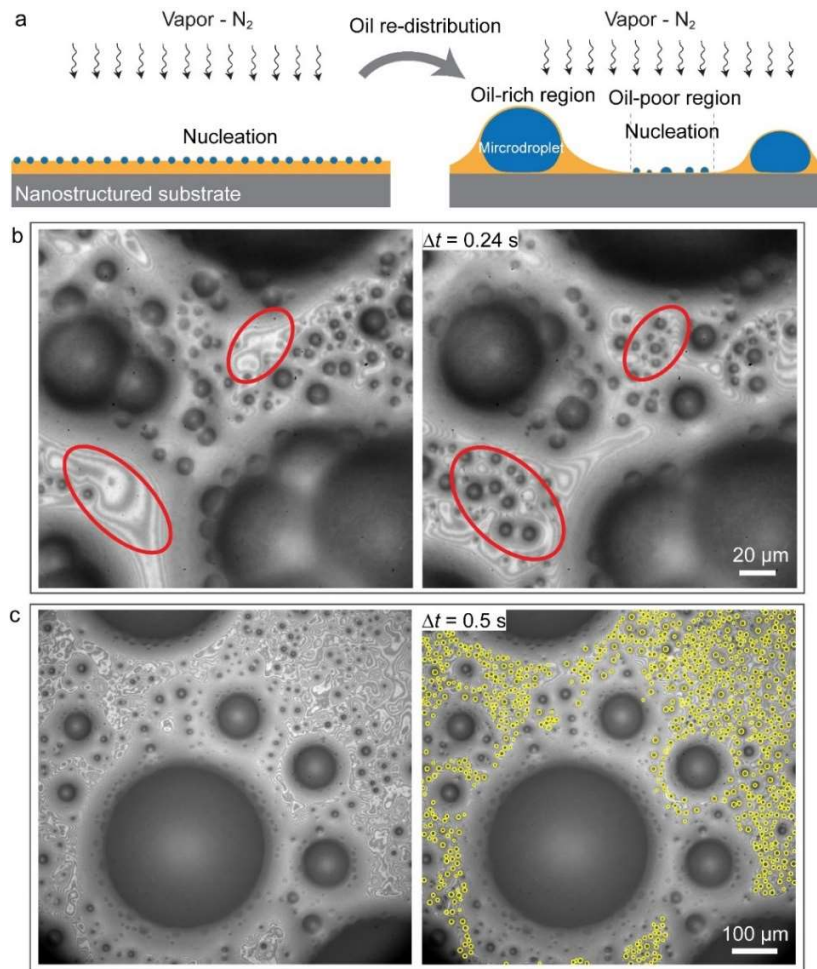


Figure 3 Schematic and experimental image sequences showing preferred nucleation in oil-poor regions. (a) Schematic of nucleation at the beginning of condensation and after the oil film re-distribution process on LIS. Subsequent generations of nucleation mainly occur in the oil-poor regions. (b) & (c) Optical imaging sequences of nucleation on a LIS with Krytox GPL 104 at the magnification of (b) $50\times$ and (c) $20\times$. Oil-poor regions are marked with red ellipses in (b). Yellow circles in (c) highlight nucleated droplets.

We can explain the preferred nucleation in the oil-poor region by combining conduction heat transfer analysis and classical nucleation theory. **Figure 4a** shows that a lower conduction resistance R_{oil} of the oil film is expected in the oil-poor regions due to a thinner layer of oil. According to Fourier's Law, we can consider the heat transfer in the oil film as one-dimensional conduction from the oil-vapor interface (temperature T_{ov}) to the colder oil-solid interface (temperature T_s):

$$q'' = k_{oil} \cdot \frac{T_{ov} - T_s}{d_{oil}}, \quad (1)$$

where q'' is the heat flux, k_{oil} the thermal conductivity of the oil, and d_{oil} the local thickness of the oil. For dropwise condensation of steam at near-atmospheric pressure, past work showed that the heat flux is typically $q'' \sim 100$ to 1500 kw/ m² [6]. Here, we make a conservative assumption of a heat flux of $q'' = 100$ kw/m² and $T_s = 276$ K. **Figure 4b** shows the change of T_{ov} with varying d_{oil} . We notice that the temperature is up to 3.5 K lower in oil-poor regions than in oil-rich regions. In the following, we will theoretically examine the influence of this thickness-induced temperature difference on nucleation. According to the classical nucleation theory (CNT), water vapor molecules diffuse to the oil-vapor interface and then form clusters which can grow only if their sizes exceed a critical size r_c . The heterogeneous nucleation rate density J (#/(m²·s)) can be calculated by [35]:

$$J = J_0 \exp\left(-\frac{\Delta G}{kT_{ov}}\right), \quad (2)$$

where J_0 is a kinetic pre-exponential factor, k is the Boltzmann constant, T_{ov} is the absolute temperature of the oil-vapor interface, and ΔG is the free-energy barrier corresponding to the critical nucleation radius r_c :

$$\Delta G = \gamma_{dv}A_{dv} + \gamma_{do}A_{do} - \gamma_{ov}\pi r_c^2 - (P_d - P_v)V_d. \quad (3)$$

In eq. (3), V_d is the volume of the nucleus, and $A_{i,j}$ are the interfacial areas between phases i and j , with the subscripts $o, d, v, ov, do,$ and dv representing the oil, droplet, vapor, oil-vapor, droplet-oil, and droplet-vapor phases, respectively. $(P_d - P_v)$ is the Laplace pressure difference between vapor and droplet. As illustrated in the schematic in **Figure 4a**, water vapor nucleates at the oil-vapor interface and the droplet can be approximated as two hemispherical caps with a deformation angle α_1 of the upper hemispherical cap and angle α_2 of the lower hemispherical cap. Hence, the interfacial areas A_{dv}, A_{do} , and the volume V_d can be described by [13,36]:

$$A_{dv} = 2\pi R_1^2(1 - \cos \alpha_1), \quad A_{do} = 2\pi R_2^2(1 - \cos \alpha_2), \quad (4)$$

$$V_d = \frac{\pi R_1^3}{3}[2 - \cos \alpha_1(2 + \sin^2 \alpha_1)] + \frac{\pi R_2^3}{3}[2 - \cos \alpha_2(2 + \sin^2 \alpha_2)], \quad (5)$$

where R_1 and R_2 are the equilibrium radii of upper and lower curvatures, respectively, and can be obtained through $R_1 \sin \alpha_1 = R_2 \sin \alpha_2 = r_c$. The critical nucleation radius and the Laplace pressure difference $(P_d - P_v)$ can be estimated respectively using [37]:

$$r_c = \frac{2\gamma_{ov}}{(P_v - P_d)} \frac{\sin \alpha_1 \sin \alpha_2}{\sin(\alpha_1 + \alpha_2)}, \quad (6)$$

$$P_d - P_v = \frac{kT_{ov}}{V_{m,d}} \ln\left(\frac{P_v}{P_{sat}}\right), \quad (7)$$

where P_{sat} and $V_{m,d}$ represent the saturation pressure and liquid molar volume at the saturation pressure, respectively.

Since Krytox oils cloak water in our three-phase (oil-water-vapor) system, the Neumann triangle law collapses. To calculate the angles α_1 and α_2 , we modified the Neumann triangle equations by replacing the interfacial tension γ_{dv} with a combined effective surface tension γ_{eff} [26,32]:

$$\cos \alpha_1 = \cos(\pi - \theta_v) = \cos \theta_v = \frac{\gamma_{d_o}^2 - \gamma_{\text{eff}}^2 - \gamma_{o_v}^2}{2\gamma_{o_v}\gamma_{\text{eff}}}, \quad (8-1)$$

$$\cos \alpha_2 = \cos \theta_o = \frac{\gamma_{\text{eff}}^2 - \gamma_{o_v}^2 - \gamma_{d_o}^2}{2\gamma_{d_o}\gamma_{o_v}}. \quad (8-2)$$

With a measured value of $\theta_v \approx 150^\circ$ for the same material system [28], the value of γ_{eff} can be determined by eq. (8-1) to $\gamma_{\text{eff}} \approx 66$ mN/m. By combining eqs. (1) and (3) – (8), we obtain the change of the free-energy barrier ΔG versus the oil film thickness d_{oil} (from oil-poor regions to oil-rich regions on LIS), corresponding to different temperatures T_{ov} , as seen in **Figure 4b**. A bulk gas temperature of $T_v = 303$ K was presumed in the calculation. We see that the energy barrier for nucleation is approximately one order of magnitude lower in oil-poor regions than in oil-rich regions, which confirms our hypothesis and initial observations that nucleation predominantly occurs in oil-poor regions.

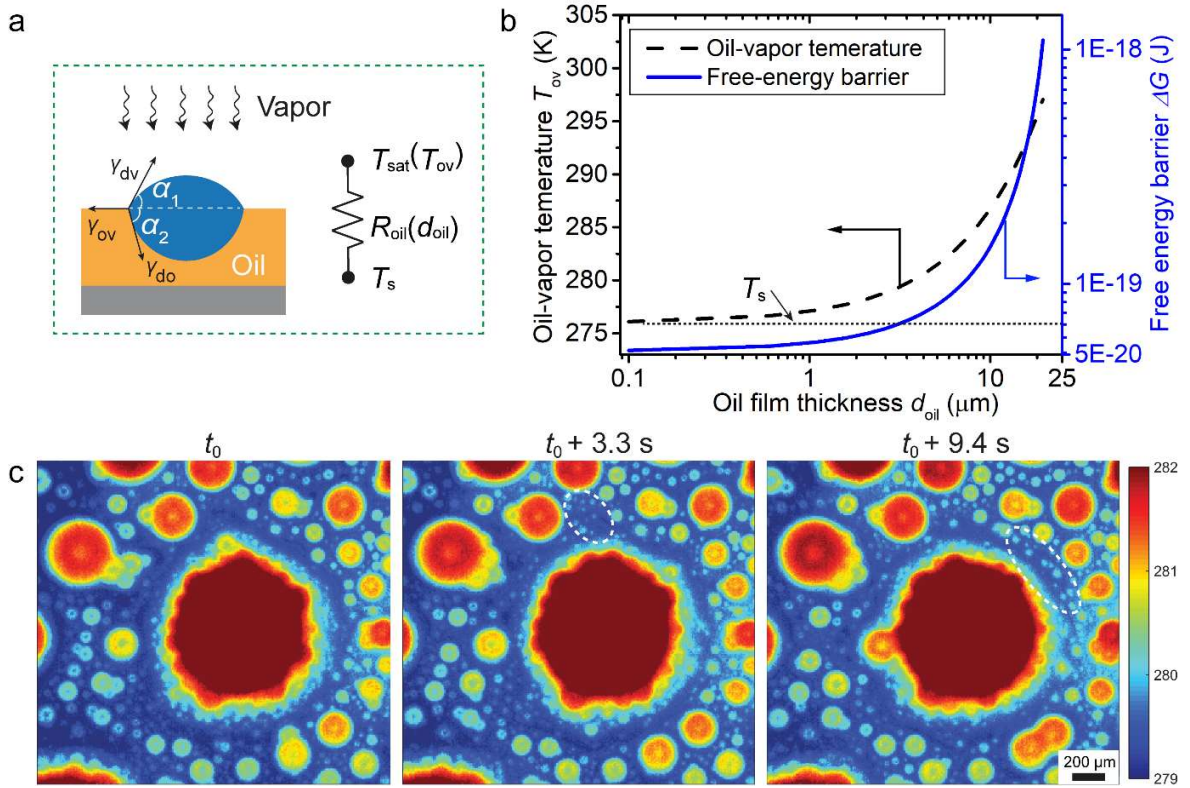


Figure 4 Thermodynamic analysis of nucleation energy barrier in oil-poor regions and thermal imaging of LIS during condensation. (a) The schematic shows the thermal path through the oil film with the conduction resistance R_{oil} . (b) Dependence of oil-vapor interfacial temperature T_{ov} (black dashed line) and free energy ΔG (blue solid line) on the oil film thickness d_{oil} . The calculation is based on the assumption of $T_s = 276$ K, $T_v = 303$ K and a heat flux $q'' = 100$ kw/m^2 . (c) Infrared image sequences in top-view, showing the temperature distribution at the oil-vapor interface during condensation. The temperature scale in Kelvin is shown without calibration for a relative comparison only. Note that the temperature in the center of the large droplet is shown as saturated to focus on the temperature distribution of the oil. The post-nucleation microdroplets are highlighted by white dashed ellipses.

To experimentally validate the calculation results, we used a Telops FAST M3k infrared camera equipped with a $4\times$ lens (Telops) at a resolution of 7.5 $\mu\text{m}/\text{pixel}$ to measure the temperature distribution of the oil-vapor interface from top-view of a LIS sample during water condensation. Heat flows from the hot vapor-saturated gas to the cold copper block that acts as a heat sink. As shown in **Figure 4c**, the surface

temperature of the droplets is highest due to the size effect on the thermal resistance. Please note that the temperature in the center of the large droplet is shown as saturated to focus on the temperature distribution of the oil. The measurement error induced by the curvature of microdroplets and oil ridges was expected to be within 1 K [37,38] and neglected in this analysis. Furthermore, note that the temperature readout has not been calibrated with respect to a blackbody radiation and serves for a relative comparison of interfacial temperatures only. In this scale, the “real” temperature of the large central droplet is approximately 285 K. The larger the radius of a droplet, the higher its temperature. An obvious temperature gradient can be seen between oil-rich regions surrounding the droplets and oil-poor regions due to the reduction in oil film thickness, which agrees well with our calculation. A number of post-nucleation microdroplets (highlighted by white dashed ellipses at $t = t_0 + 3.3$ s and 9.4 s) became visible in the fresh oil poor regions with the lowest surface temperature. Along with having a higher temperature, oil-rich regions typically surround big droplets, and the big droplets will capture more water vapor molecules, lowering the chances of cluster formation in the oil-rich regions due to vapor depletion in the gas mixture, supporting our hypothesis and observations on preferred nucleation in oil-poor regions. Similarly, this kind of “nucleation-free zone” is also reported in studies on dropwise condensation on partial/non-wetting solid surfaces [40]. It is worthy to note that nucleation is likely to occur at the oil-vapor interface in oil-rich regions only when the gas-substrate temperature difference is sufficiently high. However, this nucleation in oil-rich regions is expected to be short lasting, as nucleation releases a large amount of latent heat, leading to a fast increase in the interfacial oil-vapor temperature.

3.2 Dynamics of oil-poor regions

Since oil-poor regions are favored for nucleation, the area ratio of oil-poor regions to the total surface is expected to affect the overall nucleation rate density and thereby heat transfer performances. Previously, we reported that the location and area-ratio of oil-rich and oil-poor regions tends to dynamically change because of continuous nucleation, growth and departure of condensed droplets caused by external forces during condensation. Hence, it is essential to quantitatively investigate how the area ratio of oil-poor regions changes over time. Also, the lubricant viscosity significantly affects the movement of condensate droplets and a higher frequency and velocity of droplet movement can be achieved by choosing a low-viscosity lubricant [24,28]. Hence, the dependence of the oil-poor regions on the lubricant viscosity is worthy of further examination. We conducted condensation experiments on horizontally placed samples with GPL 102 (73 cP) and GPL 106 (1627 cP) at $T_s \approx 276$ K and $T_{\text{gas}} \approx 289$ K in an open environment. Condensed droplets with a diameter of above 450 μm slowly slid off the surface due to gas flow. Videos were analyzed to obtain the area of oil-poor regions, as shown in [Figure 5a](#). Detailed information on the analysis procedure can be found in [Section 2.3](#). The first generation of nucleating droplets is spatially uniform across the surface and submerges into the oil film due to the cloaking tendency of Krytox. Continuous growth and coalescence of droplets pulls surrounding oil towards larger droplets or droplet clusters, forming the oil-rich regions, corresponding to the dark areas in [Figures 5b, c](#). In the meantime, oil-poor regions, that is, the bright area in the images, form due to the conservation of mass of the oil phase. The droplets grow faster on the LIS with low-viscosity lubricant owing to a shorter characteristic time of coalescence [27]. As shown in [Figure 5a](#), the oil-poor regions emerge much faster on LIS with Krytox GPL 102 (lower viscosity), typically within 10 seconds of condensation, and the area of oil-poor regions quickly grows to 50% of the total surface, as a great amount of oil gathers around the rapidly growing droplets due to capillary effects. Then, this ratio gradually decreases to a quasi-steady value of about 19%, since more subsequent generations of nucleation occur in these oil-poor regions. For Krytox GPL 106 (higher viscosity), the coalescence of the initial small droplets takes significantly longer. A layer of ‘breath-figure’ water condensate droplets uniformly grow for nearly 40 seconds (at $t = 30$ s of [Figure 5c](#)). Then, the breath-figure

splits due to coalescence. The coalescence events will continuously create more oil-poor regions until the ratio stabilizes around 11% of the total surface area. Please note that these values are time-averaged, quasi-steady state values of the area ratio on the entire sample throughout the first few sweeping cycles. The local oil-poor area might decrease to zero due to the occupancy of big droplets and then be renewed by cyclic sweeping events. Over time (many hours of operation), the oil thickness and area-distribution in the oil-rich and oil-poor regions are expected to decrease because of continuous lubricant loss by the removal of condensate droplets [41]. For a solid hydrophobic surface, some studies reported that the droplet coverage typically reaches 60% of the total surface [40], but thin bands, *i.e.*, the nucleation-free zone, occur around existing drops as a result of limited vapor diffusion in the presence of NCG, which are especially pronounced around larger droplets. In our control experiments on the hydrophobic HTMS sample, the width of this nucleation-free zone was typically around 15 - 25 μm for condensate droplets. Therefore, the effective available area for nucleation on hydrophobic surfaces will comprise approximately 15% of the total surface in the steady state. Based on these findings, we hypothesize that the (re-)nucleation rate density is higher for lower viscosity oils due to a) a larger area-availability for nucleation, and b) higher droplet mobility, which can constantly create fresh oil-poor regions for nucleation.

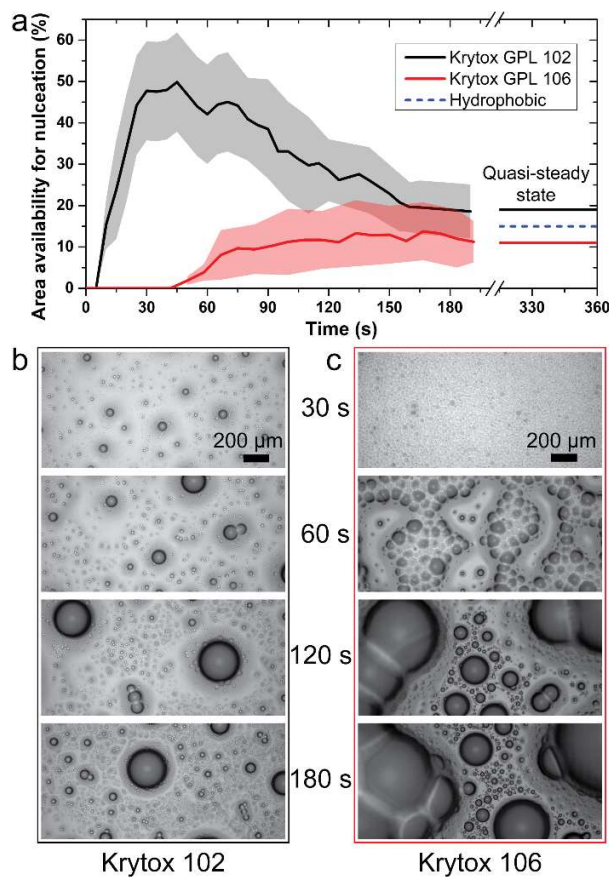


Figure 5 Time evolution of area availability for nucleation on hydrophobic and lubricant-infused surfaces with Krytox 102 and 106. (a) Formation and time evolution of oil-poor regions on LIS infused with Krytox GPL 102 (73 cP) and Krytox GPL 106 (1627 cP) at $T_s \approx 276$ K and $T_{\text{gas}} \approx 289$ K in an open environment, respectively. The shaded area represents the standard deviation of 17 individual experiments. The quasi-steady state, *i.e.*, long-term average area available for nucleation is also shown at larger times and compared to that of a solid hydrophobic surface [40]. (b) and (c) Snapshots of oil film dynamics at $t = 30$ s, 60 s, 120 s, and 180 s on LIS with (b) Krytox GPL 102 and (c) Krytox GPL 106.

3.3 Time evolution of nucleation rate density on LIS

Currently, models for the theoretical calculation of heat transfer rates during dropwise condensation are based on an integration of the per-droplet heat transfer over a static, time-averaged size distribution of droplets [6,18,42]. On LIS, the time-average condensate droplet size distribution shows no dependence on lubricant viscosity [18]. Yet experiments showed that LIS with oil of lower viscosity have a higher condensation heat transfer coefficient and a larger volume of gravity-induced shedding droplets than those on LIS with higher oil viscosity [29]. We presume that the discrepancy is attributed to the dependence of the nucleation rate density on lubricant viscosity at the basis of the influence of lubricant viscosity on the area-availability for nucleation, *i.e.*, ratio of oil-poor regions, as well as droplet mobility and coalescence rates. A high droplet nucleation rate density is key to enhancing heat transfer rates, since nearly 75% of total heat transfer happens for droplets smaller than 10 μm [18]. Hence, a macroscopic condensate droplet size distribution seems to be inadequate to represent the real nucleation and heat transfer performance on LIS. To substantiate this claim, we first examined the nucleation rate density during a full natural sweeping cycle. **Figure 6a** shows that the nucleation rate density evolves with time during a sweeping cycle in the center region of a vertically placed LIS with Krytox GPL 104, at the temperatures $T_{\text{gas}} \approx 306 \pm 2 \text{ K}$ and $T_s \approx 276 \text{ K}$. Initially, the nucleation rate density increases sharply on the surface that was refreshed by a sweeping droplet under gravity at $t = 0$, as schematically shown in **Figure 6a-i**. After achieving a maximum value of $1.1 \times 10^9 \text{ \#/m}^2\text{s}$ at $t \approx 12 \text{ s}$ (**Figure 6a-ii**), the nucleation rate density slowly decreases due to a continuous accumulation of condensate droplets, which can be considered as a quasi-steady state, as shown in the schematic of **Figure 6a-iii**. Finally, the entire area is swept again by a large droplet sliding down the surface due to gravity, and the cycle begins from the top. During quasi-steady state, local coalescence events are able to boost the nucleation rate density. At around $t = 120 \text{ s}$ (**Figure 6a-iv**), for example, as two large droplets coalesce (the smaller one gets “swallowed” by its bigger neighbor) an oil ring is left behind, in which the oil thickness is unevenly distributed: an oil-poor region in the center and an oil-rich region along the periphery of the original droplet location, which spurs a transient sharp increase in the nucleation rate density. Although the time-averaged distribution of microscopic droplet sizes on LIS follows the model developed by Rose, we observed an unceasing high nucleation rate density on the LIS due to the high mobility of condensate droplets. For dropwise condensation on the hydrophobic surface, on the contrary, the nucleation rate density was intermittent due to random coalescence events that suddenly created a large area of fresh nucleation sites. Then, the nucleation rate went to zero, until another coalescence and explosive re-nucleation event occurred.

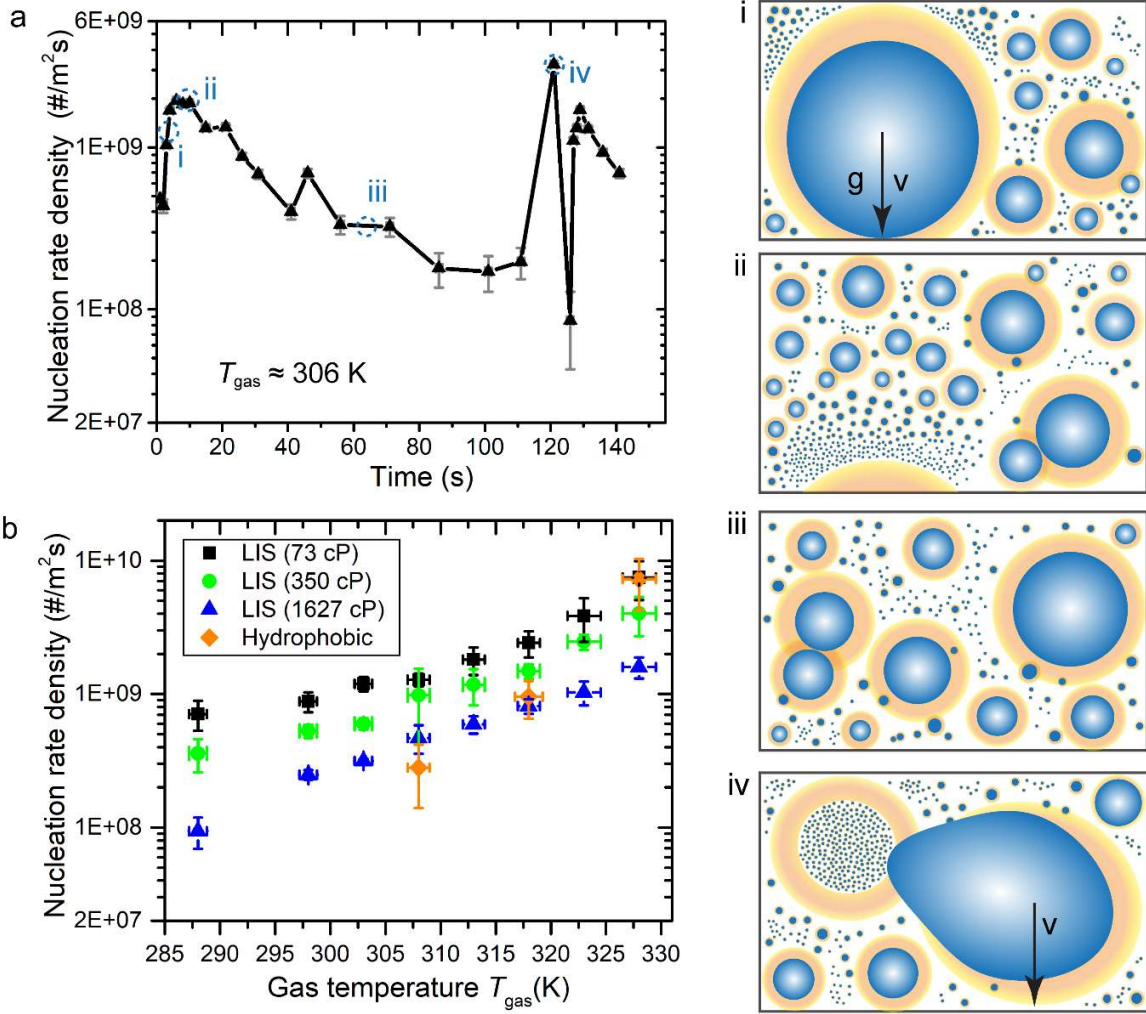


Figure 6 Time evolution of nucleation rate density (NRD) and the dependence of NRD on lubricant viscosity. (a) The NRD changes with time on a vertically placed LIS with Krytox GPL 104 at $T_{\text{gas}} \approx 306 \pm 2$ K and $T_s \approx 276$ K. The schematics (i – iv) on the right depict condensation dynamics on the LIS at different characteristic times during a condensation cycle, and are modeled after the actual video graphic signature (see supplementary video S1). (b) Dependence of nucleation rate density on lubricant viscosity at different gas temperatures T_{gas} . Data was obtained from steady-state condensation experiments on horizontally placed LIS. The nucleation rate density on vertically placed hydrophobic surfaces at select T_{gas} are also presented as a benchmark. The substrate temperature is kept constant at $T_s \approx 276$ K. The horizontal error bars are mainly from the fluctuation of gas and substrate temperatures and the vertical error bars were determined from one standard error in the mean from experiments.

3.4 Effects of lubricant viscosity and gas temperature on the nucleation rate density (NRD)

Up to now, we have shown that nucleation mainly occurs in oil-poor regions and that the area ratio of oil-poor regions can be further enhanced by lowering the lubricant viscosity. Therefore, we postulate that the nucleation rate density should differ for varying lubricant viscosities. To reveal the dependence of the nucleation rate density on lubricant viscosity, condensation experiments on LIS with Krytox GPL 102, 104, and 106 were conducted at a series of gas temperatures and a constant substrate temperature.

On a vertically placed LIS, natural sweeping rates and maximum radii of droplets before being swept are a function of the vertical location on or the tilt angle of a substrate [18]. To exclude the potential influence of orientation or measurement position on the nucleation rate density (NRD), we conducted experiments on a horizontally placed sample. By averaging the values within a natural sweeping cycle of **Figure 6a** (vertically placed sample), we obtain an average NRD of about $6.07 \times 10^8 \text{ \#/m}^2\text{s}$. The data point from **Figure 6b** (horizontally placed samples) with the same lubricant viscosity and temperature difference, but in a horizontal orientation, shows a NRD within a sweeping cycle of approximately $5.98 \times 10^8 \text{ \#/m}^2\text{s}$. Although the droplets within an artificial sweeping cycle could grow beyond the maximum size that droplets can grow within a natural sweeping cycle, we found the two values to be comparable, indicating that it is justifiable to conduct experiments on a horizontal substrate while maintaining the ability to compare results from different experiments. To elucidate the influence of lubricant viscosity and gas temperature, we averaged the mean nucleation rate density from several full artificial sweeping cycles at the respective experimental settings (for more information, see **section 2.4**) and plotted them in **Figure 6b**. Along with the results from LIS, the NRD from condensation on a vertically placed solid hydrophobic surfaces at select T_{gas} is also presented for comparison. The graph in **Figure 6b** shows that the nucleation rate density increases with gas temperature for all lubricant viscosities, as expected, since the energy barrier for heterogeneous nucleation on the oil-vapor interface decreases with the gas-substrate temperature difference according to the classical nucleation theory [43]. Importantly, we also observe that the NRD on LIS increases with decreasing viscosity. For example, a three-fold increase in NRD can be achieved by lowering the lubricant viscosity from 1627 cP to 73 cP. We attribute the enhancement to the higher area-availability for nucleation and higher mobility of condensate droplets on LIS with lower lubricant viscosity (73 cP). The total area of oil-poor regions, *i.e.*, preferential area for nucleation, is double on LIS with Krytox 102 (73 cP) than on Krytox 106 (1627 cP) (see **section 3.2**). During condensation, we noticed condensate droplets of all sizes are ‘dancing’ on LIS with low-viscosity oil (GPL 102). The frequent movement can effectively and continuously sweep the occupying droplets and leave fresh oil-poor regions behind their trajectories (compare to the schematic in **Figure 6a-iv**). As shown in **Figure 7a**, condensate droplets (outlined by dashed cyan circles) typically move long distances along the dashed lines and leave behind a large area of oil-poor regions (highlighted by red ellipses), as shown here at intervals of $\approx 0.7 \text{ s}$ on LIS with Krytox 102. Subsequently, a high density of nucleation is observed. Before gravity comes into play, the microdroplets continuously sweep the condensed droplets, which frequently exposes the colder area—previously occupied by the big droplets—to hot vapor, effectively contributing to more nucleation. For LIS with Krytox 106, on the contrary, the movement velocity is lower and the travel distances of moving droplets are much shorter, reducing the effective re-nucleation rate density.

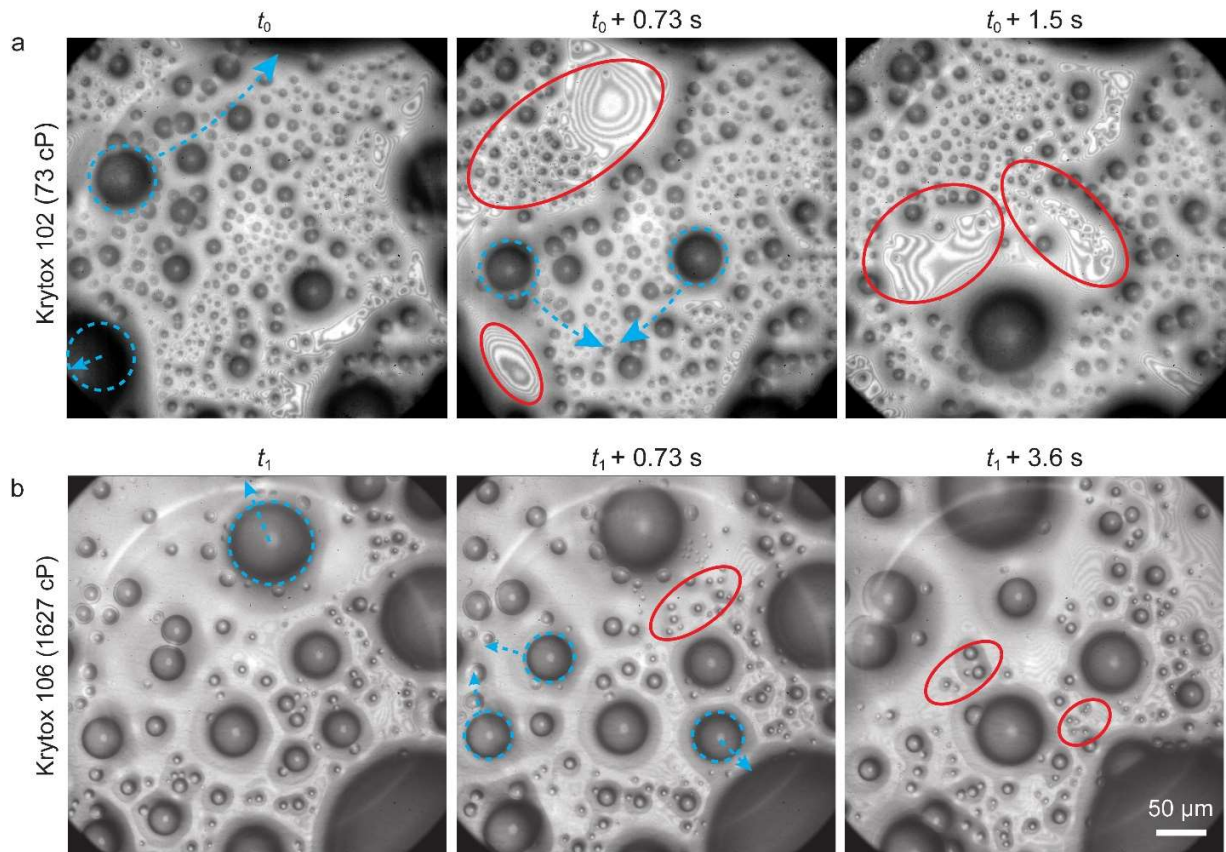


Figure 7 Image sequences of condensation on LIS with (a) Krytox 102 and (b) Krytox 106 at $T_{\text{gas}} \approx 315 \pm 2$ K and $T_s \approx 276$ K. The initial times t_0 and t_1 are randomly chosen at the beginning of the 6th sweeping cycle. Cyan color arrow lines indicate the movement and direction of droplets highlighted by cyan dash circles and the red ellipses represent the oil-poor regions with re-nucleation.

Generally, LIS can achieve higher nucleation rate densities than a solid hydrophobic surface at lower gas temperatures (< 307 K), whereas the latter seems to outperform LIS with high viscosity oils (350 cP or 1627 cP) at higher temperatures, as shown in [Figure 6b](#). During condensation at higher gas-substrate temperature differences, the characteristic time scale for individual droplet growth through direct condensation is small. At the same time, a higher viscosity oil features longer characteristic coalescence times of water droplets [27]. Thus, for LIS with higher lubricant viscosity, the rate-limiting factor for condensation becomes the coalescence and clearing of nucleation sites. At lower temperatures, however, the kinetics of nucleation and growth are rate-limiting. Hence, LIS outperform the solid hydrophobic surface due to enhanced droplet mobility and more frequent renewal of nucleation “sites”. A more detailed discussion on the influence of lubricant viscosity and lubricant thickness on condensation heat transfer rates can be found in [section 4.3](#).

4 Discussion

4.1 Influence of droplet mobility on the diffusion boundary layer of non-condensable gas

We attribute the higher nucleation rate density on lower-viscosity lubricants to two main causes: higher droplet mobility and lower coalescence times. In addition to directly clearing nucleation sites, rapid and frequent movement of droplets can potentially disturb the diffusion layer of the non-condensable gas nearby the oil-vapor interface, which facilitates the diffusion of vapor to the oil-vapor interface [44]. The non-condensable N_2 acts as carrier for water vapor to the environmental chamber in our experiments. During condensation, a thin non-condensable layer can build up near the oil-vapor interface and encompass the droplets. The accumulation of NCG not only hinders diffusion of water vapor molecules from the bulk gas mixture to the condensing surface, but also leads to a reduction in partial pressure of the vapor at the oil-vapor interface, leading to a decrease in saturation temperature. Overall, the nucleation rate density is restricted by the significant diffusion resistance of the gas-vapor boundary layer for the oils of all viscosities [34,45]. To further support the hypothesis that the frequent and fast movement of droplets can disturb the diffusion layer, we approximate the thickness of this layer using a scaling analysis based on natural convection. Here, we treat the mixture of water vapor and N_2 as air (ideal gas) in the analysis, and presume that the NCG boundary layer thickness is on the same order as the vapor concentration boundary layer thickness δ_c . The transport of water molecules is dominated by diffusion rather than convection if the Peclet number $Pe_c = U\delta_c/D < 1$, where U is the velocity of the gas mixtures and D is the mass diffusion coefficient. Provided that the gas velocity is considered as parabolic near the sample surface, the boundary layer thickness δ_c can be estimated by letting $Pe_c = 1$ [46]:

$$\delta_c \sim \left[\frac{D\delta^{\frac{3}{2}}}{4(\beta g \Delta T)^{\frac{1}{2}}} \right]^{1/3}, \quad (9)$$

where $\Delta T = T_{ov} - T_s$, β is the volume thermal expansion coefficient of air, g is the gravitational acceleration, and the hydrodynamic boundary layer thickness $\delta \sim L \cdot Gr^{-1/5} = L \cdot \left(\frac{g\beta\Delta TL^3}{\nu^2} \right)^{-1/5}$, where Gr is the Grashof number, L is the characteristic length of the sample, $L \approx 25$ mm, and ν is the kinematic viscosity. Approximating the mixture as air, we use $\nu \approx 1.6 \times 10^{-5}$ m²/s, $\Delta T = 40$ K, and $\beta = 3.43 \times 10^{-3}$ / K. These values give $Gr \approx 81,000$ and $\delta \approx 2.6$ mm with the water vapor diffusion coefficient $D = 2.42 \times 10^{-5}$ m²/s at atmospheric pressure and room temperature. Hence, at $\Delta T = 40$ K, one finds $\delta_c \approx 0.88$ mm, which is on the same order as the size of the larger droplets. Therefore, the fast movement of big condensate droplets inside the diffusion layer is expected to disturb the diffusion layer of water vapor and enhance convective vapor transport to the oil-vapor interface.

4.2 Influence of lubricant loss on nucleation and heat transfer dynamics

Continuous lubricant drainage during condensation is one of main concerns for the practical implementation of LIS in commercial thermal management applications. Some work showed that under external shear flow in microchannels a low-viscosity oil was capable of holding more oil long-term due to a smaller shear stress, but had enhanced drainage rates [47]. However, on LIS, the oil ridges surrounding condensate droplets have been recognized as the main source of lubricant loss [32]. It was also reported that a faster moving droplet with a higher driving force counterintuitively depleted less lubricant than slower-moving droplets [32]. Although there is no complete depletion globally, the performance of LIS will degrade due to the loss of oil. We assume the continuous loss of lubricant on LIS has complex and important effects on the nucleation

rate density. Tress *et al.* studied the shape of droplets and oil ridges in a slowly evaporating lubricant film and showed the size of oil menisci (or wetting ridges) is significantly smaller for a starved regime than that on LIS with excess oil [48]. Intuitively, with faster lubricant loss, we expect more oil-poor regions, *i.e.*, more available area for nucleation, which will positively enhance the nucleation density. Furthermore, the thinner oil film will result in a lower oil-vapor interfacial temperature, decreasing the nucleation energy barrier and increasing the nucleation rate. However, we cannot ignore the crucial negative aspect of smaller oil ridges: Lower mobility of droplets. We previously reported that microdroplets robustly self-propel long distances due to overlapping menisci between droplets [28]. A smaller size of oil menisci will significantly lower the probability of building wetting ‘bridges’, *i.e.*, creating overlapping menisci, between droplets. Droplets would behave as isolated islands and would not coalesce with neighboring droplets until they were much closer (*i.e.*, physically touching), similar to their behavior on a solid hydrophobic surface. This drop-off in mobility is expected to significantly decrease the refreshing rate of the surfaces occupied by condensed droplets, and hence negatively influence the nucleation rate. In this work, we attribute the higher nucleation rate density on LIS with low-viscosity oil mainly to its higher droplet mobility and coalescence rates. Hence, we expect that the nucleation rate density will decrease with loss of lubricant on LIS, yet remain superior for lower lubricant viscosity compared to higher viscosity due to typical timescales of coalescence. Similarly, in the case of pure vapor condensation, the absence of non-condensable gases and a gas diffusion layer lead to much higher condensation rates, presumably leading to faster lubricant depletion and a lower average nucleation rate density.

4.3 Comparison of heat transfer rates on LIS and solid hydrophobic surfaces

During dropwise condensation on LIS, the dynamic oil film plays an essential role in facilitating nucleation and robust self-propulsion of microdroplets. Nonetheless, the oil film adds an extra thermal resistance between the substrate and droplets as compared to a solid hydrophobic surface. To evaluate the influence of the lubricant thickness on the overall heat transfer, we model the dropwise condensation heat transfer and compare it to a hydrophobic surface. The steady state condensation heat flux (q'') is obtained by integrating the individual droplet heat transfer rate q_d over the steady-state average droplet size distribution $N(r)$ [42]:

$$q'' = \int_{r_{\min}}^{r_e} q_d(r)n(r)dr + \int_{r_e}^{r_{\max}} q_d(r)N(r)dr . \quad (10)$$

Here, the values of nucleation rate density (NRD, $\#/(m^2 \cdot s)$) from our current experiments (**Fig. 6b**) can be considered as the approximate number of droplets with radii in the interval $r \sim [r_0, r_0 + dr]$ on a condensing area with a unit of $(\#/m^2)$, where $r_0 \approx 1.5 \mu m$ is the radius of the smallest visible droplet and $dr \approx 0.8 \mu m$ is the uncertainty in detecting droplets. Then, the probability density $n(r)$ for small droplets with radii $r_{\min} < r < r_e$ can be obtained by $n(r) = \text{NRD}/dr$ ($\#/m^3$). The minimum, temperature-dependent critical radius r_{\min} is given by [30]:

$$r_{\min} = \frac{2T_{\text{sat}}\gamma_{\text{dv}}}{\Delta h_{\text{fg}}\rho_d(T_{\text{sat}} - T_s)} , \quad (11)$$

where Δh_{fg} is the latent heat of condensation and ρ_d is the water droplet density. The radius r_e is the effective transition radius from the direct condensation to the coalescence dominated growth regime, which is determined from the experiment observation with the consideration of $n(r_e) = N(r_e)$. For larger droplets with $r_e < r < r_{\max}$, the number density $N(r)$ on solid hydrophobic surfaces was developed by Rose and co-workers [6,18]:

$$N(r) = \frac{1}{3\pi r r_{\max}} \left(\frac{r}{r_{\max}} \right)^{-2/3}, \quad (12)$$

where r_{\max} is the radius of the largest droplets before shedding and can be calculated based on the force balance between surface tension and external forces, such as gravity [6,18,42]. In our experiments of **Fig. 6b**, $r_{\max} \approx 0.39$ mm. For LIS, the droplet size distribution is given by [18]:

$$N(r) = 6 \times 10^7 r^{-3.05}. \quad (13)$$

For a single droplet on LIS, as shown in **Figure 8a**, the thermal network model includes several temperature drops: $\Delta T_c = (T_{\text{sat}} - T_s) \cdot r_{\text{min}}/r$ due to the droplet curvature effect, ΔT_i because of the droplet-vapor interfacial resistance R_i , ΔT_d due to the conduction resistance through the droplet, R_d , ΔT_{oil} due to the conduction resistance through the oil, R_{oil} , and ΔT_{str} caused by the resistance of the Glaco nanostructures associated with the lubricant resistance R_{str} . The single droplet heat transfer rate on LIS is [18]:

$$q_d = \frac{\Delta T_c + \Delta T_i + \Delta T_d + \Delta T_{\text{oil}} + \Delta T_{\text{str}}}{R_i + R_d + R_{\text{oil}} + R_{\text{str}}} = \frac{\pi r (T_{\text{sat}} - T_s) \left(1 - \frac{r_{\text{min}}}{r}\right)}{\frac{1}{2h_i} + \frac{r\theta_A}{4k_d \sin \theta_A} + \frac{d_{\text{oil}}}{k_{\text{oil}}} + \frac{\delta_{\text{glaco}}}{k_{\text{eff}}}}, \quad (14)$$

where θ_A is the apparent water contact angle, $\delta_{\text{glaco}} (\approx 1 \mu\text{m})$ is the thickness of the Glaco coating, d_{oil} is the lubricant thickness between the droplet and the nanostructures, and k_d and k_{oil} are the thermal conductivities of the droplet (water) and the lubricant (Krytox oil), respectively. k_{eff} is the effective thermal conductivity of the nanostructure layer filled with lubricant,

$$k_{\text{eff}} = k_{\text{glaco}} \left[\frac{k_{\text{oil}} + 2k_{\text{glaco}} - 2f(k_{\text{glaco}} - k_{\text{oil}})}{k_{\text{oil}} + 2k_{\text{glaco}} + f(k_{\text{glaco}} - k_{\text{oil}})} \right], \quad (15)$$

where f is the solid surface fraction in the coating layer. Here, f was estimated to 0.3. For our analysis, we vary the total coating thickness ($d_{\text{oil}} + \delta_{\text{glaco}}$) to examine the influence of the lubricant layer beneath the droplets on the overall heat transfer rate. For the heat transfer rate of a condensing droplet on the hydrophobic surface (not shown here), the third and fourth terms in the denominator of Eq. (14) are negligible.

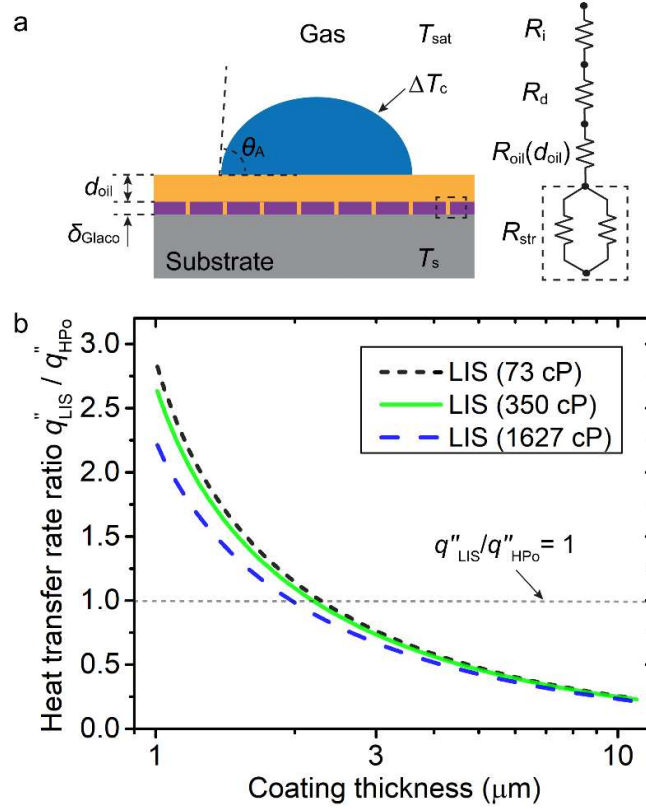


Figure 8 Comparison of heat transfer rates. (a) Schematic of a thermal network through a condensing droplet on LIS. It includes interfacial resistance R_i , and three conduction resistances through the droplet R_d , the lubricant layer R_{oil} , and a combined resistance R_{str} from the nanostructures filled with lubricant. (b) Influence of total coating thickness (Glaco and lubricant) of LIS on the overall heat transfer rate for the different lubricant viscosities, in comparison to the heat transfer during dropwise condensation on a solid hydrophobic surface.

As can be seen from **Figure 8b**, the decreased nucleation energy barrier, enhanced droplet mobility, and high nucleation rate density on LIS can enhance condensation heat transfer rates as compared to a solid hydrophobic surface. However, for coating thicknesses (Glaco + excess lubricant) exceeding $\approx 2 \mu m$, the added thermal resistance negatively influences the heat transfer for water condensation on LIS. As expected, the heat transfer performance declines with increasing lubricant thickness due to a higher thermal resistance of the lubricant layer. The thickness of the sandwiched lubricant layer between droplet and the Glaco surface likely approximates to the local oil film thickness at the beginning of nucleation (**Figure 4a**), but we assume that it would quickly decrease to the microscale ($\sim \delta_{Glaco} \approx 1 \mu m$) once the nuclei grow to microdroplets, as past research showed the equilibrium oil film thickness beneath a $1 \mu l$ droplet on a flat surface is $25 \pm 5 \text{ nm}$ [49]. Based off **Figure 8b**, while lubricant viscosity has a slight effect on the overall heat transfer, other considerations, such as lubricant depletion and droplet coalescence ability should be prioritized when designing lubricant-infused surfaces for condensation heat transfer applications. We also note that the comparison in **Figure 8b** represents water condensation. However, when liquids with lower surface tension, such as hydrocarbons or alcohols, are considered, LIS should always be the preferred choice, since – unlike LIS – conventional hydrophobic surfaces do not promote stable dropwise condensation of these liquids [11]. Furthermore, we note that the conventional model for dropwise condensation might not be applicable to accurately predict heat transfer on LIS. In the future, a more comprehensive mathematical model is highly desired to incorporate features of oil menisci around droplets,

the varying oil film thickness, droplet clustering, and – more importantly – the high mobility of condensed droplets and the influence of lubricant viscosity on coalescence times. A long-lasting lubricant coating with a relatively high thermal conductivity for LIS application is in urgent demand. For example, an active oil replenishing system for a LIS condenser was recently proposed and able to maintain dropwise condensation for > 48 hours under high supersaturation levels [50].

5 Conclusions

In this work, we showed that nucleation is limited to the oil-poor regions and highly dependent on the lubricant viscosity during water condensation on LIS. Using a 1D thermal conduction model through the oil film, we showed that the temperature at the oil-vapor interface is lower in the oil-poor regions than the oil-rich regions, which was also confirmed using infrared imaging. Based on Gibbs' thermodynamics analysis, even a small temperature difference can significantly affect nucleation because of an exponential temperature dependence of the nucleation barrier energy. We also found that the area ratio of oil-poor regions dynamically changes with time. By lowering the lubricant viscosity from 1627 to 73 cP, we observed that the average area ratio of oil-poor regions increases from 11% to 19%. Then, we experimentally examined the dependence of the nucleation rate density on lubricant viscosity at a wide range of gas-substrate temperature differences. The results showed the nucleation rate density is proportional to the temperature difference, in agreement with the classical nucleation theory. At a given temperature difference, higher nucleation rate densities could be achieved by lowering the lubricant viscosity. This increase can be attributed to a) a larger area available for re-nucleation (that is, higher ratio of oil-poor regions), and b) a higher frequency and speed of condensate movement of droplets of all sizes on LIS with lower viscosity Krytox oils. Microdroplets spontaneously move towards relatively bigger droplets, that is, oil-rich regions. The robust movement can efficiently refresh the surface by sweeping all droplets in the trajectories of the moving droplets and then leave an empty oil-poor region behind for new nucleation. At the same time, using scale analysis we argue that the movement can also disturb the non-condensable gas / vapor diffusion boundary layer and thereby enhance the nucleation rate density. At low gas-substrate temperatures, LIS with all lubricant viscosities (73 cP – 1627 cP) showed higher nucleation rate densities than a solid hydrophobic benchmark surface, however, LIS with high viscosity oils (350 cP and 1627 cP) underperformed due to lesser area-availability for nucleation and low mobility and coalescence rates at larger temperature differences. The majority of nucleation density values reported in previous experimental studies were measured at the beginning of the condensation and do not account for both the spatial and temporal component of dynamic re-nucleation, whereas we demonstrate the importance of the re-nucleation rate density spanning an artificial sweeping cycle. Through discussion on lubricant depletion and heat transfer rates we highlight the importance of careful and diligent lubricant selection. These findings could be helpful to comprehensively understand the interplay of the lubricant film and nucleation, and to enhance nucleation rate density and heat transfer performance by tailoring the lubricant viscosity.

Conflicts of interest

We report no conflicts of interest.

Acknowledgement

The authors would like to thank Michael Lorberg for assisting with droplet counting, and Jonathan Boreyko for elucidating discussions. The work was supported by the National Science Foundation, Grant No. 1856722. The authors acknowledge the use of instruments and staff assistance from the Institute of Materials Science and Engineering (IMSE), the Nano Research Facility (NRF), and the Jens Environmental Analysis Facility at Washington University in St. Louis.

References

- [1] L. Zhai, M.C. Berg, F.Ç. Cebeci, Y. Kim, J.M. Milwid, M.F. Rubner, R.E. Cohen, Patterned Superhydrophobic Surfaces: Toward a Synthetic Mimic of the Namib Desert Beetle, *Nano Lett.* 6 (2006) 1213–1217. <https://doi.org/10.1021/nl060644q>.
- [2] V.G. Reifert, A.I. Sardak, S.V. Grigorenko, V.L. Podbereznyj, Heat exchange at dropwise condensation in heat exchangers of desalination plants, *Desalination.* 74 (1989) 373–382. [https://doi.org/10.1016/0011-9164\(89\)85064-7](https://doi.org/10.1016/0011-9164(89)85064-7).
- [3] N. Lukic, L.L. Diezel, A.P. Fröba, A. Leipertz, Economical aspects of the improvement of a mechanical vapour compression desalination plant by dropwise condensation, *Desalination.* 264 (2010) 173–178. <https://doi.org/10.1016/j.desal.2010.07.023>.
- [4] R. Kehlhofer, *Combined-cycle Gas & Steam Turbine Power Plants*, PennWell Books, 1999.
- [5] N.A. Patankar, Supernucleating surfaces for nucleate boiling and dropwise condensation heat transfer, *Soft Matter.* 6 (2010) 1613–1620. <https://doi.org/10.1039/B923967G>.
- [6] J.W. Rose, Dropwise condensation theory and experiment: A review, *Proceedings of the Institution of Mechanical Engineers, Part A: Journal of Power and Energy.* 216 (2002) 115–128. <https://doi.org/10.1243/09576500260049034>.
- [7] R. Enright, N. Miljkovic, J.L. Alvarado, K. Kim, J.W. Rose, Dropwise Condensation on Micro- and Nanostructured Surfaces, *Nanoscale and Microscale Thermophysical Engineering.* 18 (2014) 223–250. <https://doi.org/10.1080/15567265.2013.862889>.
- [8] X. Chen, J. Wu, R. Ma, M. Hua, N. Koratkar, S. Yao, Z. Wang, Nanograssed Micropyramidal Architectures for Continuous Dropwise Condensation, *Adv. Funct. Mater.* 21 (2011) 4617–4623. <https://doi.org/10.1002/adfm.201101302>.
- [9] Y. Hou, M. Yu, X. Chen, Z. Wang, S. Yao, Recurrent Filmwise and Dropwise Condensation on a Beetle Mimetic Surface, *ACS Nano.* 9 (2015) 71–81. <https://doi.org/10.1021/nn505716b>.
- [10] T.-S. Wong, S.H. Kang, S.K.Y. Tang, E.J. Smythe, B.D. Hatton, A. Grinthal, J. Aizenberg, Bioinspired self-repairing slippery surfaces with pressure-stable omniphobicity, *Nature.* 477 (2011) 443–447. <https://doi.org/10.1038/nature10447>.
- [11] D.J. Preston, Z. Lu, Y. Song, Y. Zhao, K.L. Wilke, D.S. Antao, M. Louis, E.N. Wang, Heat Transfer Enhancement During Water and Hydrocarbon Condensation on Lubricant Infused Surfaces, *Scientific Reports.* 8 (2018) 1–9. <https://doi.org/10.1038/s41598-017-18955-x>.
- [12] M. Villegas, Y. Zhang, N. Abu Jarad, L. Soleymani, T.F. Didar, Liquid-Infused Surfaces: A Review of Theory, Design, and Applications, *ACS Nano.* 13 (2019) 8517–8536. <https://doi.org/10.1021/acsnano.9b04129>.

- [13] F. Eslami, J.A.W. Elliott, Thermodynamic Investigation of the Barrier for Heterogeneous Nucleation on a Fluid Surface in Comparison with a Rigid Surface, *The Journal of Physical Chemistry B*. 115 (2011) 10646–10653. <https://doi.org/10.1021/jp202018e>.
- [14] L. Yang, X. Quan, P. Cheng, Z. Cheng, A free energy model and availability analysis for onset of condensation on rigid and liquid surfaces in moist air, *International Journal of Heat and Mass Transfer*. 78 (2014) 460–467. <https://doi.org/10.1016/j.ijheatmasstransfer.2014.07.006>.
- [15] M. Sokuler, G.K. Auernhammer, M. Roth, C. Liu, E. Bonaccorso, H.-J. Butt, The Softer the Better: Fast Condensation on Soft Surfaces, *Langmuir*. 26 (2010) 1544–1547. <https://doi.org/10.1021/la903996j>.
- [16] R. Xiao, N. Miljkovic, R. Enright, E.N. Wang, Immersion Condensation on Oil-Infused Heterogeneous Surfaces for Enhanced Heat Transfer, *Sci. Rep.* 3 (2013). <https://doi.org/10.1038/srep01988>.
- [17] S. Anand, A.T. Paxson, R. Dhiman, J.D. Smith, K.K. Varanasi, Enhanced Condensation on Lubricant-Impregnated Nanotextured Surfaces, *ACS Nano*. 6 (2012) 10122–10129. <https://doi.org/10.1021/nn303867y>.
- [18] P.B. Weisensee, Y. Wang, H. Qian, D. Schultz, W.P. King, N. Miljkovic, Condensate droplet size distribution on lubricant-infused surfaces, *International Journal of Heat and Mass Transfer*. 109 (2017) 187–199. <https://doi.org/10.1016/j.ijheatmasstransfer.2017.01.119>.
- [19] A. Kiselev, F. Bachmann, P. Pedevilla, S.J. Cox, A. Michaelides, D. Gerthsen, T. Leisner, Active sites in heterogeneous ice nucleation—the example of K-rich feldspars, *Science*. 355 (2017) 367–371. <https://doi.org/10.1126/science.aai8034>.
- [20] K.K. Varanasi, T. Deng, Controlling nucleation and growth of water using hybrid hydrophobic-hydrophilic surfaces, in: *IEEE*, 2010: pp. 1–5. <https://doi.org/10.1109/ITHERM.2010.5501324>.
- [21] S. Anand, K. Rykaczewski, S.B. Subramanyam, D. Beysens, K.K. Varanasi, How droplets nucleate and grow on liquids and liquid impregnated surfaces, *Soft Matter*. 11 (2015) 69–80. <https://doi.org/10.1039/C4SM01424C>.
- [22] T. Kajiya, F. Schellenberger, P. Papadopoulos, D. Vollmer, H.-J. Butt, 3D Imaging of Water-Drop Condensation on Hydrophobic and Hydrophilic Lubricant-Impregnated Surfaces, *Scientific Reports*. 6 (2016) 23687. <https://doi.org/10.1038/srep23687>.
- [23] P. Kim, M.J. Kreder, J. Alvarenga, J. Aizenberg, Hierarchical or Not? Effect of the Length Scale and Hierarchy of the Surface Roughness on Omniphobicity of Lubricant-Infused Substrates, *Nano Lett.* 13 (2013) 1793–1799. <https://doi.org/10.1021/nl4003969>.
- [24] J.D. Smith, R. Dhiman, S. Anand, E. Reza-Garduno, R.E. Cohen, G.H. McKinley, K.K. Varanasi, Droplet mobility on lubricant-impregnated surfaces, *Soft Matter*. 9 (2013) 1772–1780. <https://doi.org/10.1039/C2SM27032C>.
- [25] F. Schellenberger, J. Xie, N. Encinas, A. Hardy, M. Klapper, P. Papadopoulos, H.-J. Butt, D. Vollmer, Direct observation of drops on slippery lubricant-infused surfaces, *Soft Matter*. 11 (2015) 7617–7626. <https://doi.org/10.1039/C5SM01809A>.
- [26] C. Semprebon, G. McHale, H. Kusumaatmaja, Apparent contact angle and contact angle hysteresis on liquid infused surfaces, *Soft Matter*. 13 (2017) 101–110. <https://doi.org/10.1039/C6SM00920D>.

- [27] J.B. Boreyko, G. Polizos, P.G. Datskos, S.A. Sarles, C.P. Collier, Air-stable droplet interface bilayers on oil-infused surfaces, *Proceedings of the National Academy of Sciences*. 111 (2014) 7588–7593. <https://doi.org/10.1073/pnas.1400381111>.
- [28] J. Sun, P.B. Weisensee, Microdroplet self-propulsion during dropwise condensation on lubricant-infused surfaces, *Soft Matter*. 15 (2019) 4808–4817. <https://doi.org/10.1039/C9SM00493A>.
- [29] H. Tsuchiya, M. Tenjimbayashi, T. Moriya, R. Yoshikawa, K. Sasaki, R. Togasawa, T. Yamazaki, K. Manabe, S. Shiratori, Liquid-Infused Smooth Surface for Improved Condensation Heat Transfer, *Langmuir*. 33 (2017) 8950–8960. <https://doi.org/10.1021/acs.langmuir.7b01991>.
- [30] X. Liu, P. Cheng, Dropwise condensation theory revisited Part II. Droplet nucleation density and condensation heat flux, *International Journal of Heat and Mass Transfer*. 83 (2015) 842–849. <https://doi.org/10.1016/j.ijheatmasstransfer.2014.11.008>.
- [31] A.G. Emslie, F.T. Bonner, L.G. Peck, Flow of a Viscous Liquid on a Rotating Disk, *Journal of Applied Physics*. 29 (1958) 858–862. <https://doi.org/10.1063/1.1723300>.
- [32] M.J. Kreder, D. Daniel, A. Tetreault, Z. Cao, B. Lemaire, J.V.I. Timonen, J. Aizenberg, Film Dynamics and Lubricant Depletion by Droplets Moving on Lubricated Surfaces, *Phys. Rev. X*. 8 (2018) 031053. <https://doi.org/10.1103/PhysRevX.8.031053>.
- [33] D. Bonn, J. Eggers, J. Indekeu, J. Meunier, E. Rolley, Wetting and spreading, *Rev. Mod. Phys.* 81 (2009) 739–805. <https://doi.org/10.1103/RevModPhys.81.739>.
- [34] W.J. Minkowycz, E.M. Sparrow, Condensation heat transfer in the presence of noncondensables, interfacial resistance, superheating, variable properties, and diffusion, *International Journal of Heat and Mass Transfer*. 9 (1966) 1125–1144. [https://doi.org/10.1016/0017-9310\(66\)90035-4](https://doi.org/10.1016/0017-9310(66)90035-4).
- [35] A. Aleksandrov, B. Toshev, A. Sheludko, Nucleation from supersaturated water vapors on n-hexadecane: temperature dependence of critical supersaturation and line tension, *Langmuir*. 7 (1991) 3211–3215. <https://doi.org/10.1021/la00060a048>.
- [36] A.D. Alexandrov, B.V. Toshev, A.D. Scheludko, Nucleation from supersaturated water vapour on immiscible liquid substrates: Effect of the macroscopic geometry of the three-phase system on the critical supersaturation and the line tension, *Colloids and Surfaces A: Physicochemical and Engineering Aspects*. 79 (1993) 43–50. [https://doi.org/10.1016/0927-7757\(93\)80158-B](https://doi.org/10.1016/0927-7757(93)80158-B).
- [37] A.A. Nepomnyashchy, A.A. Golovin, A.E. Tikhomirova, V.A. Volpert, Nucleation and growth of droplets at a liquid-gas interface, *Phys. Rev. E*. 74 (2006) 021605. <https://doi.org/10.1103/PhysRevE.74.021605>.
- [38] A. Chandramohan, J.A. Weibel, S.V. Garimella, Spatiotemporal infrared measurement of interface temperatures during water droplet evaporation on a nonwetting substrate, *Appl. Phys. Lett.* 110 (2017) 041605. <https://doi.org/10.1063/1.4975003>.
- [39] T.-Y. Cheng, D. Deng, C. Herman, CURVATURE EFFECT QUANTIFICATION FOR IN-VIVO IR THERMOGRAPHY, *Int Mech Eng Congress Expo*. 2 (2012). <https://doi.org/10.1115/IMECE2012-88105>.
- [40] R.N. Leach, F. Stevens, S.C. Langford, J.T. Dickinson, Dropwise Condensation: Experiments and Simulations of Nucleation and Growth of Water Drops in a Cooling System, *Langmuir*. 22 (2006) 8864–8872. <https://doi.org/10.1021/la061901+>.
- [41] S. Sett, P. Sokalski, K. Boyina, L. Li, K.F. Rabbi, H. Auby, T. Foulkes, A. Mahvi, G. Barac, L.W. Bolton, N. Miljkovic, Stable Dropwise Condensation of Ethanol and Hexane

- on Rationally Designed Ultrascalable Nanostructured Lubricant-Infused Surfaces, *Nano Lett.* 19 (2019) 5287–5296. <https://doi.org/10.1021/acs.nanolett.9b01754>.
- [42] S. Kim, K.J. Kim, Dropwise Condensation Modeling Suitable for Superhydrophobic Surfaces, *J. Heat Transfer.* 133 (2011). <https://doi.org/10.1115/1.4003742>.
- [43] D. Kashchiev, *Nucleation: Basic theory with applications*, Butterworth Heinemann, Oxford and Boston, 2000.
<http://search.ebscohost.com/login.aspx?direct=true&scope=site&db=nlebk&db=nlabk&AN=207508>.
- [44] R. Wen, X. Zhou, B. Peng, Z. Lan, R. Yang, X. Ma, Falling-droplet-enhanced filmwise condensation in the presence of non-condensable gas, *International Journal of Heat and Mass Transfer.* 140 (2019) 173–186.
<https://doi.org/10.1016/j.ijheatmasstransfer.2019.05.110>.
- [45] P.F. Peterson, V.E. Schrock, T. Kageyama, Diffusion Layer Theory for Turbulent Vapor Condensation With Noncondensable Gases, *J. Heat Transfer.* 115 (1993) 998–1003.
<https://doi.org/10.1115/1.2911397>.
- [46] M.-G. Medici, A. Mongruel, L. Royon, D. Beysens, Edge effects on water droplet condensation, *Phys. Rev. E.* 90 (2014) 062403.
<https://doi.org/10.1103/PhysRevE.90.062403>.
- [47] J.S. Wexler, I. Jacobi, H.A. Stone, Shear-Driven Failure of Liquid-Infused Surfaces, *Phys. Rev. Lett.* 114 (2015) 168301. <https://doi.org/10.1103/PhysRevLett.114.168301>.
- [48] M. Tress, S. Karpitschka, P. Papadopoulos, J.H. Snoeijer, D. Vollmer, H.-J. Butt, Shape of a sessile drop on a flat surface covered with a liquid film, *Soft Matter.* 13 (2017) 3760–3767. <https://doi.org/10.1039/C7SM00437K>.
- [49] D. Daniel, J.V.I. Timonen, R. Li, S.J. Velling, J. Aizenberg, Oleoplaning droplets on lubricated surfaces, *Nature Phys.* 13 (2017) 1020–1025. <https://doi.org/10.1038/nphys4177>.
- [50] D. Seo, J. Shim, C. Lee, Y. Nam, Brushed lubricant-impregnated surfaces (BLIS) for long-lasting high condensation heat transfer, *Scientific Reports.* 10 (2020) 1–13.
<https://doi.org/10.1038/s41598-020-59683-z>.